

# Visualization and analysis of stochastic Lorenz'63 by means of computing the quasipotential

Maria Cameron<sup>\*1</sup> and Shuo Yang<sup>†1</sup>

<sup>1</sup>Department of Mathematics, University of Maryland, College Park, MD 20742, USA

December 15, 2024

## Abstract

The ordered line integral method (OLIM) for computing the quasipotential is a powerful tool for visualization and analysis of dynamical systems perturbed by small white noise. It allows one to depict the sets explored by the system on various timescales. In systems with multiple attractors, it facilitates the study of noise-induced transitions between various basins. Maximum likelihood escape paths and estimates for expected escape times from basins of attractions are readily obtained once the quasi-potential is calculated. In this work, we present an application of the OLIM to the stochastic Lorenz'63 model with  $\sigma = 10$ ,  $\beta = 8/3$ , and  $\rho$  ranging from 0.5 to 24.4. Our 3D computations show that for  $\rho \gtrsim 15$  the dynamics of the system are virtually restricted to a small neighborhood of certain 2D sets on moderately large timescales. We have developed a technique to extract these 2D sets and generate meshes on them. We have adjusted the 2D OLIM for radial meshes and performed refined computations on these manifolds or unions of manifolds. We compare two transition mechanisms from the strange attractor to a stable spiral point at  $\rho = 24.4$  and show that the quasipotential barriers associated with them are relatively small and close to each other. Our C source codes for computing the quasi-potential for Lorenz'63 in 2D and 3D and a collection of Matlab programs are posted on M. Cameron's web page. Some presented 3D figures are supplemented with movies.

## 1 Introduction

The Lorenz'63 system

$$\begin{aligned}\dot{x} &= \sigma(y - x), \\ \dot{y} &= x(\rho - z) - y, \\ \dot{z} &= xy - \beta z\end{aligned}\tag{1}$$

is one of the most fascinating and transformative ODE models proposed in the twentieth century. E. Lorenz [19] derived it from Saltzman's 2D cellular convection model [22] using a Fourier expansion and truncating the trigonometric series to include a total of three terms. He proved that the resulting system exhibits a new type of long-term behavior. All trajectories of (1) stay in a bounded

---

<sup>\*</sup>cameron@math.umd.edu

<sup>†</sup>shuoyang@math.umd.edu

region. For  $\sigma = 10$ ,  $\beta = 8/3$ , and  $\rho = 28$ , their  $\omega$ -limit sets form an “infinite complex of surfaces”, i.e., a fractal, whose Hausdorff dimension is 2.06 [28], later named the Lorenz attractor. The Lorenz map [19], a 1D map  $z_{n+1} = f(z_n)$  where  $z_n$  is the  $n$ th maximum of the  $z$ -component of a trajectory, explained the divergence of arbitrarily close characteristics. It has become instrumental for analysis of chaotic dynamical systems.

The study of the Lorenz’63 system bursted in mid-1970s, perhaps due to the progress in the computer industry. A number of remarkable properties and quantitative characteristics have been discovered. The topological structure of the Lorenz attractor was studied in [12, 21, 29]. The phenomenon called preturbulence was described in [18]. The value of  $\rho \approx 24.06$  at which the Lorenz attractor is born for  $\sigma = 10$  and  $\beta = 8/3$  was found in [30] using a functional fit to the Lorenz map. Homoclinic explosions, period-doubling cascades, and periodicity windows were investigated in [24]. A beautiful overview of the Lorenz system is given in [26] (Chapters 9–12). Nowadays, the Lorenz system is a popular test model for new methods in such fields as machine learning and forecasting (e.g. [11, 23, 13]).

In this work, we consider the Lorenz system perturbed by small white noise:

$$d\mathbf{x} = \begin{bmatrix} \sigma(x_2 - x_1) \\ x_1(\rho - x_3) - x_2 \\ x_1x_2 - \beta x_3 \end{bmatrix} dt + \sqrt{\epsilon} d\mathbf{w}, \quad \text{where} \quad \mathbf{x} \equiv \begin{bmatrix} x_1 \\ x_2 \\ x_3 \end{bmatrix}, \quad (2)$$

$d\mathbf{w}$  is the three-dimensional standard Brownian motion, and  $\epsilon$  is a small parameter. We set  $\sigma = 10$  and  $\beta = 8/3$ , and let  $\rho$  range from zero to the critical value  $\rho_2 \approx 24.74$  at which the strange attractor becomes the only attractor of the corresponding deterministic ODE (1). The noise term regularizes the chaotic deterministic dynamics of (1) in the sense that one can predict the future probability density function given the current one by solving the Fokker-Planck equation. On the other hand, the presence of the noise term enables escapes from any neighborhood of an attractor of (1). If  $\rho$  is such that there are multiple attractors, noise-induced transitions between their neighborhoods become possible.

If  $\epsilon$  is sufficiently small, asymptotic estimates for the probability measure in the neighborhoods of attractors, expected escape times, and maximum likelihood escape paths are offered by the large deviation theory (LDT) [14] in terms of the function called the *quasipotential*. Unfortunately, the quasipotential can be found analytically only for some special classes of SDEs, e.g., for linear SDEs [6, 7]. SDE (2) does not admit an analytic form of the quasipotential.

In this work, we apply the recently introduced 3D quasipotential solver [31] to SDE (2) and visualize its dynamics. These computations show that level sets of the quasipotential become thin as  $\rho$  increases. This fact indicates that the dynamics of SDE (2) on the corresponding timescales are virtually restricted to small neighborhoods of sets that can be approximated by 2D manifolds or unions of two 2D manifolds. We develop a technique to construct these 2D manifolds and perform refined 2D computations of the quasipotential on them. We study transitions between the stable equilibria of (1) at  $\rho = 12, 15$ , and 20, and them and the strange attractor at  $\rho = 24.4$ . At  $\rho = 24.4$ , we compare two transition mechanisms from the strange attractor to the equilibria.

Our 2D and 3D computations are done by the Dijkstra-like ordered line integral method (OLIM) with the midpoint quadrature rule [9, 31]. The technical challenge in applying these methods to SDE (2) is caused by the fact that the magnitude of the rotational component of the vector field in the right-hand side of (1) grows dramatically in comparison with that of the potential component. The ratio between them almost reaches  $10^3$  at  $\rho = 24.4$ . To address this issue, we have adjusted the 2D OLIM for radial meshes on manifolds and demonstrated a superquadratic decay of the

normalized maximal absolute error with mesh refinement for a test problem mimicking the one we face in our 2D computations for (2).

Aiming at making our results readily reproducible, we have made most of the codes developed for this project publicly available at M. Cameron’s web page [5] – see the package `Qpot4lorenz63.zip`. A user guide for the codes is also provided there.

The rest of the paper is organized as follows. In Section 2, some necessary background on the quasipotential is given. A brief overview of the dynamics of Lorenz’63 (1) at  $\sigma = 10$ ,  $\beta = 8/3$ , and  $0 < \rho < \infty$  is offered in Section 3. Numerical techniques for computing the quasipotential are described in Section 4. The application of the quasipotential solvers to Lorenz’63 is presented in Section 5. We summarize our findings in Section 6. Some technicalities are explained in Appendices A, B, and C.

## 2 Definition and significance of the quasipotential

We consider SDEs of the form

$$d\mathbf{x} = \mathbf{b}(\mathbf{x})dt + \sqrt{\epsilon}d\mathbf{w}. \quad (3)$$

To understand what is the quasipotential [14], we first assume that the vector field  $\mathbf{b}(\mathbf{x})$  admits the following smooth orthogonal decomposition:

$$\mathbf{b}(\mathbf{x}) = -\frac{1}{2}\nabla u(\mathbf{x}) + \mathbf{l}(\mathbf{x}), \quad \nabla u(\mathbf{x}) \cdot \mathbf{l}(\mathbf{x}) = 0. \quad (4)$$

The term  $-(1/2)\nabla u(\mathbf{x})$  is the potential component of  $\mathbf{b}(\mathbf{x})$ , and  $\mathbf{l}(\mathbf{x})$  is its rotational component.

If the field  $\mathbf{b}(\mathbf{x})$  were gradient, i.e.,  $\mathbf{l}(\mathbf{x}) \equiv \mathbf{0}$ , the Gibbs measure

$$\mu(\mathbf{x}) = Z^{-1}e^{-u(\mathbf{x})/\epsilon}. \quad (5)$$

would be the invariant probability density for SDE (3). Suppose  $\mathbf{l}(\mathbf{x})$  is not identically zero. Plugging the Gibbs measure into the stationary Fokker-Planck equation for SDE (3)

$$\frac{1}{2}\Delta\mu(\mathbf{x}) - \nabla \cdot (\mu(\mathbf{x})\mathbf{b}(\mathbf{x})) = 0 \quad (6)$$

we find that it is invariant provided that the rotational component  $\mathbf{l}(\mathbf{x})$  is divergence-free, i.e.,  $\nabla \cdot \mathbf{l}(\mathbf{x}) \equiv 0$ . In this case, the function  $u(\mathbf{x})$  would play the role of a potential.

Unfortunately, the orthogonal decomposition (4) where  $\mathbf{l}(\mathbf{x})$  is divergence-free does not typically exist. However, a function  $U(\mathbf{x})$  called the quasipotential that gives asymptotic estimates for the invariant probability measure near attractors of  $\dot{\mathbf{x}} = \mathbf{b}(\mathbf{x})$  in the limit  $\epsilon \rightarrow 0$  can be designed [14].

Suppose that the vector field  $\mathbf{b}(\mathbf{x})$  is continuously differentiable. In addition, we assume that the ODE

$$\dot{\mathbf{x}} = \mathbf{b}(\mathbf{x}) \quad (7)$$

has a finite number of attractors, and every trajectory of (7) remains in a bounded region. Let  $A$  be an attractor of (7). The quasipotential with respect to  $A$  is defined as the solution of the following minimization problem

$$U(\mathbf{x}) = \inf_{\phi, T_0, T_1} \{S_{T_0, T_1}(\phi) \mid \phi(T_0) \in A, \phi(T_1) = \mathbf{x}\}, \quad (8)$$

where the infimum of the Freidlin-Wentzell action

$$S_{T_0, T_1}(\phi) = \frac{1}{2} \int_{T_0}^{T_1} \|\dot{\phi} - \mathbf{b}(\phi)\|^2 dt. \quad (9)$$

is taken over the set of absolutely continuous paths  $\phi$  with endpoints at the attractor  $A$  and  $\mathbf{x}$ , and all times  $T_0, T_1 \in \mathbb{R}$ . The infimum with respect to  $T_0$  and  $T_1$  can be taken analytically [14, 15, 16] resulting in the geometric action

$$S(\psi) = \int_0^L (\|\psi'\| \|\mathbf{b}(\psi)\| - \psi' \cdot \mathbf{x}(\psi)) ds, \quad (10)$$

where the path  $\psi$  is parametrized by its arclength, and  $L$  is the length of  $\psi$ . As a result, the definition of the quasipotential can be rewritten in terms of the geometric action:

$$U(\mathbf{x}) = \inf_{\psi} \{S(\psi) \mid \phi(0) \in A, \phi(L) = \mathbf{x}\}. \quad (11)$$

Using Bellman's principle of optimality [2], one can show [4] that the quasipotential  $U(\mathbf{x})$  satisfies the Hamilton-Jacobi equation

$$\frac{1}{2} \|\nabla v(\mathbf{x})\|^2 + \mathbf{b}(\mathbf{x}) \cdot \nabla v(\mathbf{x}) = 0. \quad (12)$$

Note that the orthogonality of  $\mathbf{l}$  and  $\nabla u$  in equation (4) implies that  $u$  must satisfy the same Hamilton-Jacobi equation (12) [14].

We remark that the boundary value problem (BVP) defined by (12) with the boundary condition (BC)  $v(A) = 0$  is ill-posed. It always has a trivial solution  $v(\mathbf{x}) \equiv 0$  and may or may not have a smooth nontrivial solution. The quasipotential defined by (8) or (11) is a viscosity solution [8] to this BVP. The other complication is that even a nontrivial solution to this BVP, classical or viscosity, may not be unique due to the fact that the boundary condition is imposed on an attractor [17]. For example, if  $\mathbf{b}(\mathbf{x}) = B\mathbf{x}$  where  $B$  is a matrix with all eigenvalues having negative real parts, the number of solutions of (12) with the BC  $u(\mathbf{0}) = 0$  is equal to the number of invariant subspaces for  $B$ .

Nonetheless, (12) is instrumental in deriving an equation for *minimum action paths* (MAPs) a.k.a. *maximum likelihood paths* or *instantons* that minimize the geometric action (10) [14, 4]:

$$\psi'(s) = \frac{\mathbf{b}(\psi(s)) + \nabla U(\psi(s))}{\|\mathbf{b}(\psi(s)) + \nabla U(\psi(s))\|}. \quad (13)$$

MAPs can be found e.g. using the geometric minimum action method (GMAM) [15, 16], an iterative path-based method requiring an initial guess for the path. Alternatively, once the quasipotential is computed, one can shoot a MAP from a given point  $\mathbf{x}$  back to the attractor  $A$  by integrating (13) backward in  $s$ .

The mentioned asymptotic estimate for the invariant probability density within a level set of the quasipotential completely lying in the basin  $\mathcal{B}(A)$  of  $A$  is [14]

$$\mu(\mathbf{x}) \asymp e^{-U(\mathbf{x})/\epsilon}, \quad (14)$$

where the symbol  $\asymp$  denotes the logarithmic equivalence. The expected escape time from  $\mathcal{B}(A)$  can also be estimated up to exponential order [14]:

$$\mathbb{E}[\tau_{\mathcal{B}(A)}] \asymp e^{U(\mathbf{x}^*)/\epsilon}, \quad \text{where } U(\mathbf{x}^*) = \min_{\mathbf{x} \in \partial \mathcal{B}(A)} U(\mathbf{x}). \quad (15)$$



In some common special cases, a sharp estimate for the expected escape time can be obtained [3].

The term *transition state* is often encountered in chemical physics literature. Mostly it refers to a Morse index one saddle lying on the manifold separating two basins of attraction. The dynamics of the Lorenz system (1) are complicated, and basins of its attractors are tightly interlaced for  $\rho \gtrsim 20$ . To accommodate such situations, we will define the term *escape state*.

**Definition 2.1.** *Consider a system evolving according to an SDE (3). Let  $A$  be an attractor of the corresponding ODE  $\dot{\mathbf{x}} = \mathbf{b}(\mathbf{x})$ . The escape state from  $A$  is the set of points minimizing the quasipotential with respect to  $A$  over the boundary of the basin of  $A$ .*

Therefore, the quasipotential at the escape state from  $A$  defines the expected escape time from the basin of  $A$  up to exponential order according to Eq. (15).

### 3 A brief overview of Lorenz'63

In this Section, we remind the reader some key facts regarding the dynamics of the Lorenz system (1). It is easy to check that (1) is invariant under the symmetry transformation  $(x_1, x_2, x_3) \mapsto (-x_1, -x_2, x_3)$ . Let us fix the parameters  $\sigma = 10$  and  $\beta = 8/3$ . As  $\rho$  grows from zero to infinity, the dynamics of (1) go through a number of bifurcations [18, 24, 25, 26]:

- For all  $0 < \rho < \infty$ , the origin is a fixed point of (1). It is the only equilibrium for  $0 < \rho < 1$ , and it is globally attracting. At  $\rho = 1$ , a supercritical pitchfork bifurcation occurs transforming the origin into a Morse index one saddle and giving birth to two equilibria

$$C_{\pm} = \left( \pm \sqrt{\beta(\rho - 1)}, \pm \sqrt{\beta(\rho - 1)}, \rho - 1 \right). \quad (16)$$

They remain asymptotically stable for  $1 < \rho < \rho_2 \approx 24.74$ . The unstable manifold of the Lorenz system (1) linearized near the saddle at the origin for  $1 < \rho < \infty$  is the span of the vector

$$\xi = \begin{bmatrix} \frac{\sigma}{2} \\ \frac{\sigma-1}{2} + \sqrt{\left(\frac{\sigma+1}{2}\right)^2 + \sigma(\rho-1)} \\ 0 \end{bmatrix}. \quad (17)$$

To delineate the evolution of the dynamics of (1) as  $\rho$  grows from 1 to infinity, we have plotted the bifurcation diagram displayed in Fig. 1. For each  $\rho$  from 1.05 to 349.95 with step 0.1, we traced the trajectory starting at  $10^{-2}\xi$  for time  $0 \leq t \leq 200$  and recorded its points of intersection with the horizontal plane  $\alpha$  passing through the equilibria  $C_{\pm}$ . The  $x_1$ -components of these intersects are shown with pink dots in the  $(\rho, x_1)$ -plane. The time interval  $0 \leq t \leq 200$  is large enough for this trajectory to approach an attractor. Then, in order to depict  $x_1$ -components of the intersection of the attractor with the plane  $\alpha$ , we continued tracing the trajectory for  $200 \leq t \leq 400$  and plotted the  $x_1$  components of its intersects with  $\alpha$  with red dots. The corresponding sets of points for the trajectory starting at  $-10^{-2}\xi$  are obtained using the aforementioned symmetry of (1). They are plotted with grey and black dots respectively.

- For  $1 < \rho < \rho_0 \approx 13.926$ , the characteristics emanating from the saddle at the origin along the directions  $\xi$  and  $-\xi$  approach, respectively,  $C_+$  and  $C_-$  without crossing the plane  $x_1 = 0$  (see Fig. 1).

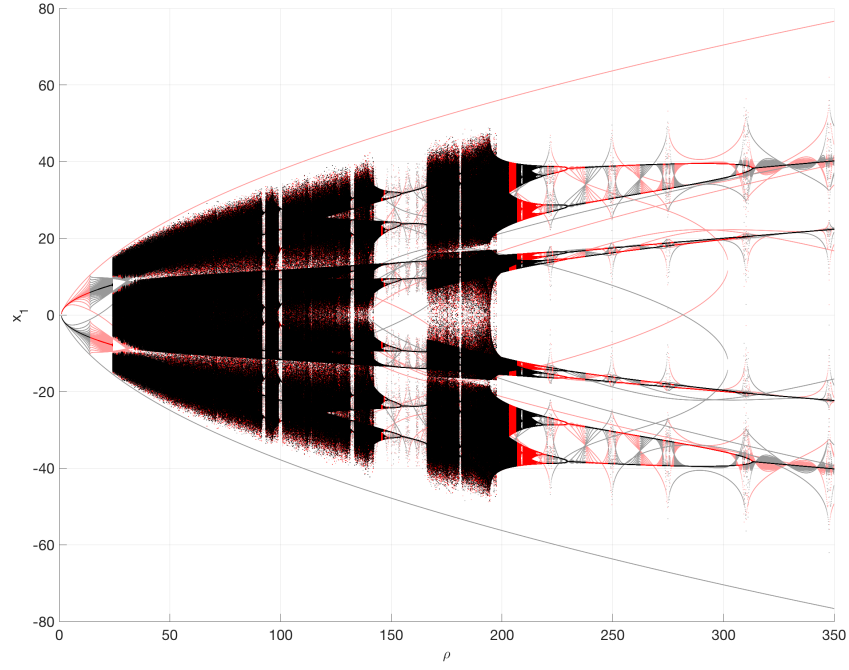


Figure 1: Consider the characteristics of (1) emanating from the origin along the directions  $\xi$  and  $-\xi$  and traced for the time interval  $0 \leq t \leq 200$ . The  $x_1$ -components of their intersections with the horizontal plane passing through the equilibria  $C_{\pm}$  are plotted for  $1 \leq \rho \leq 350$  with pink and grey dots respectively. Then each characteristic is continued to be traced for  $200 \leq t \leq 400$ . The resulted  $x_1$  components of their intersections with the same plane are marked with red and black respectively. The dashed green vertical lines correspond to the critical values of rho:  $\rho_0 \approx 13.926$ ,  $\rho_1 \approx 24.06$ , and  $\rho_2 \approx 24.74$ .

- The interval  $\rho_0 \approx 13.926 < \rho < \rho_2 \approx 24.74$  is marked by the existence of the saddle limit cycles  $\gamma_+$  and  $\gamma_-$  surrounding  $C_+$  and  $C_-$  respectively. The equilibria  $C_{\pm}$  remain the only attractors for  $\rho_0 < \rho < \rho_1 \approx 24.06$ . At  $\rho = \rho_0$ , there exist homoclinic orbits emanating from the origin and approaching it at  $t \rightarrow \infty$ . For all  $\rho_0 < \rho < \rho_1$ , the characteristics emanating from the origin along the directions  $\xi$  and  $-\xi$  go about half-way around the limit cycles, cross the plane  $x_1 = 0$ , and approach  $C_-$  and  $C_+$  respectively (see Fig. 1). As  $\rho$  grows within this interval, there develops a phenomenon called *preturbulence* [18], characterized by chaotic behavior and divergence of close characteristics. For example, characteristics starting near  $\gamma_+$  on the outer side of it on the cone  $\Upsilon_+$  consisting of all rays starting at  $C_+$  and crossing  $\gamma_+$ , i.e.,

$$\Upsilon_+ := \{C_+ + t(\mathbf{x} - C_+) \mid t \geq 0, \mathbf{x} \in \gamma_+\}, \quad (18)$$

perform more and more revolutions around  $C_+$  and  $C_-$  prior they settle to spiraling near one of the stable equilibria. Moreover, it is getting progressively harder and finally impossible to predict using double-precision arithmetic which equilibrium such a characteristic will eventually approach as  $\rho$  tends to  $\rho_1$ . An example of two characteristics for  $\rho = 20$  starting at two close points near  $\gamma_+$  on the cone  $\Upsilon_+$  and eventually approaching different equilibria is shown in Fig. 2. At  $\rho = \rho_1$ , the characteristics emanating from the origin along the directions  $\xi$  and  $-\xi$  approach  $\gamma_-$  and  $\gamma_+$  respectively. This gives birth to a strange attractor a.k.a. the Lorenz attractor. We will denote it by  $A_L$  where “L” stands for “Lorenz”. The critical value  $\rho_1 \approx 24.06$  was found in [30] by means of fitting a certain class of functions to the Lorenz map.

- For  $\rho_1 \approx 24.06 < \rho < \rho_2 \approx 24.74$ , there are three attractors: the strange attractor, and the asymptotically stable equilibria  $C_{\pm}$ . The characteristics emanating from the origin along  $\pm\xi$  miss the saddle cycles  $\gamma_{\mp}$  respectively and start spiraling away from them.  $\gamma_{\pm}$  lie on the boundaries of the basins of  $C_{\pm}$  respectively and, as we show in Section 5.4, play roles of the escape states from  $C_{\pm}$  to  $A_L$ . At  $\rho = \rho_2$ , the saddle cycles  $\gamma_{\pm}$  shrink to the corresponding equilibria  $C_{\pm}$  rendering them unstable, i.e., a subcritical Hopf bifurcation takes place.
- For  $\rho_2 \approx 24.74 < \rho < \infty$ , the dynamics is complicated as can be inferred from Fig. 1.  $A_L$  is the only attractor for some open interval of  $\rho$  starting at  $\rho_2$ . It exists for a union of intervals of  $\rho$  stretching up to approximately  $\rho = 215.364$  [24]. The interval  $p_2 < \rho \lesssim 215.364$  is cut through by a number of windows of periodicity where there exist attracting limit cycles. The largest of them is  $145 \lesssim \rho \lesssim 166$ . Some other ones are located around  $\rho = 93$ ,  $\rho = 100$ ,  $\rho = 133$ , and  $\rho = 181.5$ . Zooming in, we can spot more windows of periodicity and reveal cascades of period doublings marking the Feigenbaum scenarios of transition to chaos. The final doubling period interval is  $215.364 \lesssim \rho \lesssim 313$  [24] clearly visible in Fig. 1. Near  $\rho = 313$ , two symmetric attracting limit cycles merge into one resulting in the final limit cycle that remains the only attractor for all larger values of  $\rho$ .

## 4 Numerical methods

The family of ordered line integral methods (OLIMs) for computing the quasipotential for 2D SDEs of the form (3) on regular rectangular meshes was introduced in [9]. They have been extended for position-dependent and anisotropic diffusion in [10] and promoted to 3D in [31]. The OLIMs are Dijkstra-like algorithms that advance the computation of the quasipotential roughly from smaller values to larger values without iteration. At each step of the OLIMs, the functional minimization

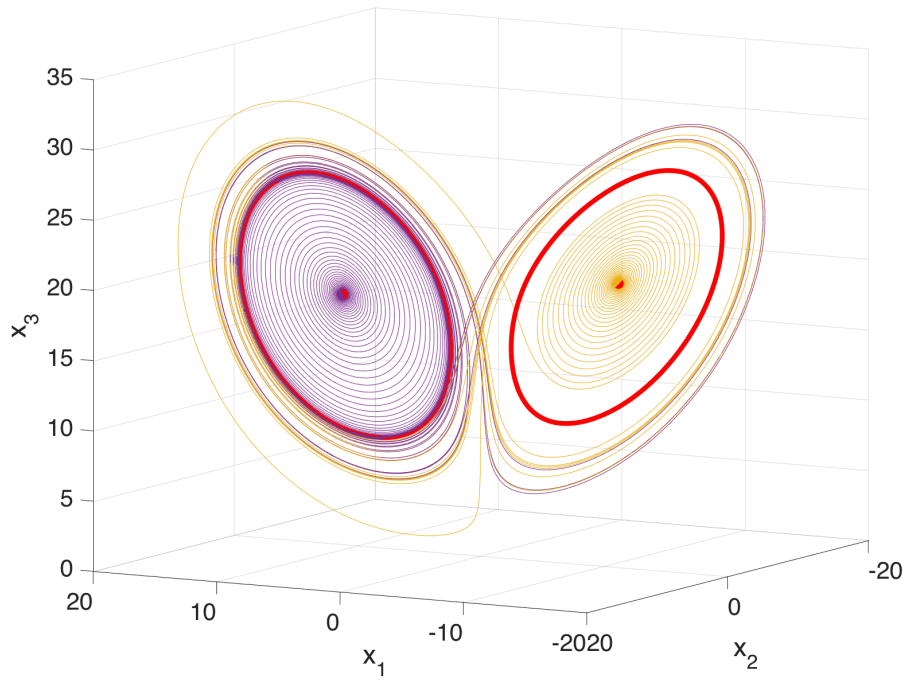


Figure 2: (a): An example of two characteristics at  $\rho = 20$  starting at two close points lying near  $\gamma_+$  on the cone with vertex at  $C_+$  and consisting of all rays passing through  $\gamma_+$  and eventually diverging and approaching different equilibria.

problem (10)–(11) is solved locally. The minimizer of each local subproblem is sought among straight line paths, and the geometric action along them is approximated by a quadrature rule. The best results are often achieved when the midpoint rule is used, so we stick with it in this work. The OLIMs were shown to be superior to the first quasipotential solver [4] as they are both significantly faster, have error constants smaller by two to three orders of magnitude, and may exhibit faster convergence rates. We are referring interested reader to [9, 31] where detailed descriptions on the OLIMs in 2D and 3D are available. Here we focus on adjustments that have been made to address specific challenges of computing the quasipotential for the Lorenz system.

#### 4.1 Radial meshes on manifolds

We have computed the quasipotential for the Lorenz system at a number of values of  $\rho$ . One of the challenges that we have encountered as we have been increasing  $\rho$  is the dramatic growth of the ratio of the magnitude of the rotational component to that of the rotational one:

$$\Xi(\mathbf{x}) := \frac{\|\mathbf{l}(\mathbf{x})\|}{\|^{1/2}\nabla U(\mathbf{x})\|}. \quad (19)$$

This ratio for the Lorenz system at  $1 < \rho < \rho_2 \approx 24.74$  can be estimated from that for the linearized system at  $C_+$  (see Appendix A). The graph of  $\Xi$  for the linearized system is displayed in Fig. 3. It shows that the ratio blows up as  $\rho \rightarrow \rho_2$ . At  $\rho = 24.4$ , the largest  $\rho$  at which we present the results of our computations, the maximal value of  $\Xi(\mathbf{x})$  for the linearized system is 973.4.

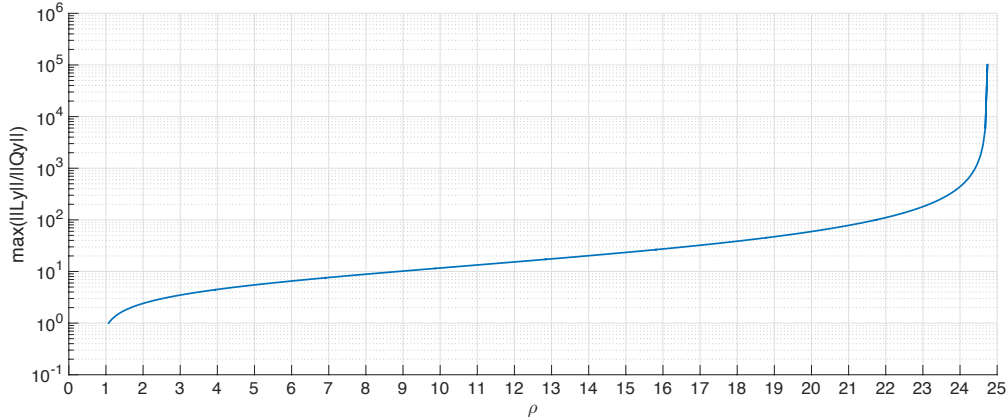


Figure 3: The graph of the maximal ratio  $\Xi$  of the magnitudes of the rotational and potential components of the linear SDE  $d\mathbf{y} = J\mathbf{y}dt + \sqrt{\epsilon}d\mathbf{w}$  where the matrix  $J$  is the Jacobian matrix of the right-hand side of the Lorenz system (1) evaluated at the asymptotically stable  $C_+$ . The range  $1 < \rho < \rho_2 \approx 24.74$  is such that  $C_+$  is asymptotically stable.

The 3D quasipotential solver [31] was tested for  $\Xi \leq 10$ . The measurements and the analysis conducted in [31] suggest that, as this ratio increases, there is a bad news that error constants also increase but also a good news that the effective order of convergence becomes superlinear. Therefore, for the values of  $\rho$  where  $\Xi(\mathbf{x}) \gg 10$ , error constants in our 3D computations of the quasipotential can be large. Since the computer memory is limited, we cannot use too large mesh sizes. Therefore, the results of 3D computations on rectangular meshes for large  $\rho$  can give only qualitative idea about the behavior of the quasipotential, but the actual numbers are not trustworthy.

On the other hand, there is a very helpful fact associated with the increase of  $\rho$ . As we will see in Section 5, level sets of the quasipotential thin out and the sets of characteristics and MAPs form 2D manifolds lying very close to each other. This gives us an idea to neglect the difference between these manifolds and perform 2D computations of the quasipotential on the manifold consisting of characteristics that can be readily constructed.

In particular, we will perform 2D computations on manifolds formed by all characteristics going from the limit cycle  $\gamma_+$  to the corresponding asymptotically stable equilibrium  $C_+$ . The high curvature of MAPs spiraling away from  $C_+$  bears large errors on rectangular meshes. To abate this issue, we build radial meshes. We call a mesh radial if it is set up as follows. Let  $\gamma_0$  be a point or a closed curve, and let  $\gamma$  be another closed curve. We pick a finite set of simple closed curves that do not intersect pairwise and index them  $\gamma_i$ ,  $i = 1, \dots, N_r - 2$ . We add  $\gamma_0$  and  $\gamma_{N_r-1} \equiv \gamma$  to this set. These curves will be referred to as *parallels*. We also pick a finite set of curves, *meridians*, going from  $\gamma_0$  to  $\gamma$  and crossing each  $\gamma_i$  exactly once in the order of increase of their indices. We index the meridians from 0 to  $N_a - 1$  and identify meridian 0 with meridian  $N_a$ . The resulting mesh has size  $N_r \times N_a$ . Examples of radial meshes for the Lorenz system defined on manifolds consisting of all characteristics going from saddle cycles to asymptotically stable equilibria at  $\rho = 15$  and  $\rho = 24.4$  are shown in Figs. 8(a) and 13(a) respectively. A radial mesh defined between two closed curves, the saddle cycle  $\gamma_-$  and a closed curve approximating an “eye” of the strange attractor at  $\rho = 24.4$ , is displayed in Fig. 14(a). Our technique for building radial meshes is described in Appendix B.

A very important parameter for the OLIMs on rectangular meshes is the update factor  $K$  defining the radius of the neighborhood from which a mesh point can be updated [9, 31]. For radial meshes, such update neighborhood  $\mathcal{N}_{\text{far}}(i_r, i_a)$  of a point indexed  $(i_r, i_a)$  is defined by two update factors,  $K_r$  and  $K_a$ , and consists of all mesh points  $(j_r, j_a)$  satisfying

$$\max\{0, i_r - K_r\} \leq j_r \leq \min\{i_r + K_r, N_r - 1\} \quad \text{and} \\ |(j_a - i_a) \bmod N_a| \leq K_a.$$

Let us check whether our quasipotential solver applied to a system with large ratio  $\Xi$  produces small enough errors on 2D radial meshes of reasonable sizes and these errors properly decay with mesh refinement. We set up an ad hoc 2D example with an asymptotically stable spiral point at the origin and an unstable limit cycle  $\|\mathbf{x}\| = 1$  where  $\Xi \geq 10^3$ :

$$\begin{bmatrix} dx_1 \\ dx_2 \end{bmatrix} = \begin{bmatrix} \|\mathbf{x}\|^2 - 1 & 10^3 \\ -10^3 & \|\mathbf{x}\|^2 - 1 \end{bmatrix} \begin{bmatrix} x_1 \\ x_2 \end{bmatrix} dt + \sqrt{\epsilon} d\mathbf{w}. \quad (20)$$

The exact quasipotential for (20) with respect to the origin is given by

$$U(\mathbf{x}) = \begin{cases} \|\mathbf{x}\|^2 (1 - 0.5\|\mathbf{x}\|^2) & \|\mathbf{x}\| \leq 1 \\ 0.5, & \|\mathbf{x}\| > 1 \end{cases}. \quad (21)$$

We have conducted two experiments with computing the quasipotential for (20). The goal of the first experiment is to establish the dependence of the numerical error on the relationship between  $N_r$ ,  $N_a$ , and  $K_r$ . We set  $N_r = 1024$  and run the solver for  $N_a = 2^q N_r$ ,  $q = 0, 1, 2, 3$ , and  $K_r$  varying from 1 to  $\text{round}(N_r/40) = 25$  and  $K_a = 2^q K_r$ , respectively. The computational domain is the unit circle. The dependence of the normalized maximal absolute error

$$E := \frac{\max_{i_r, i_a} |U(i_r, i_a) - U_{\text{exact}}(i_r, i_a)|}{\max_{i_r, i_a} U_{\text{exact}}(i_r, i_a)} \quad (22)$$

on  $K_r$  is shown in Fig. 4(a). The normalized maximal absolute error for the  $1024 \times 1024$  rectangular mesh defined on the unit square (the red curve) is also provided for comparison. These results eloquently demonstrate the superiority of the radial meshes for computing the quasipotential in the case where the ratio  $\Xi$  is large. We also observe that it is advantageous to choose  $N_a$  at least twice as large as  $N_r$ . Finally, the choice  $K_r = \text{round}(N_r/40)$  and  $K_a = \text{round}(N_a/40)$  is reasonable and can be used as a default setting for radial meshes.

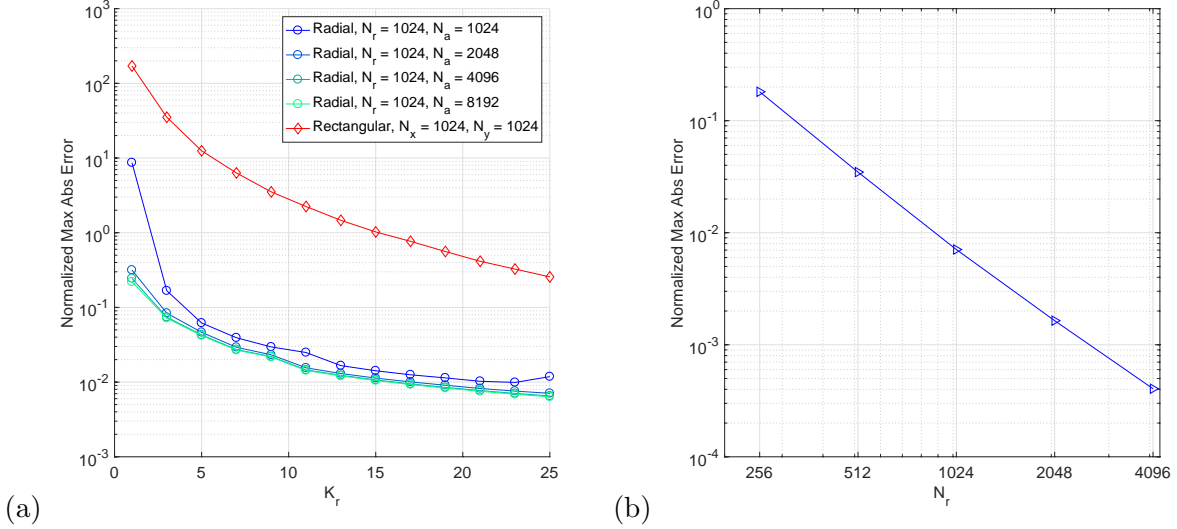


Figure 4: Measurements of numerical errors for radial meshes  $N_r \times N_a$  in computing the quasipotential for SDE (20). (a): The dependence of the normalized maximal absolute error (22) on the update parameter  $K_r$ . The parameter  $K_a$  was chosen so that  $N_a/N_r = K_a/K_r$ . (b): The dependence of the normalized maximal absolute error (22) on  $N_r$  with  $N_a = 2N_r$ ,  $K_r = \text{round}(N_r/40)$ , and  $K_a = 2K_r$ .

The goal of the second experiment is to verify error decay with mesh refinement. We have run computations with  $N_r = 2^p$ ,  $p = 8, 9, 10, 11, 12$ ,  $N_a = 2N_r$ ,  $K_r = \text{round}(N_r/40)$ , and  $K_a = 2K_r$ . The plot of the normalized maximal absolute error in Fig. 4(b) shows the desired convergence. The least squares fit gives a superquadratic coverage:

$$E = 3.3 \cdot 10^4 \cdot N_r^{-2.2}. \quad (23)$$

Therefore, our experiment with SDE (20) with a stable spiral point and an unstable limit cycle and  $\Xi \geq 10^3$  demonstrated that the computation of the quasipotential on radial meshes of moderate sizes gives accurate and reliable results.

## 5 Results

In this section, we present a collection of plots of the level sets of the computed quasipotential in 3D for the Lorenz system at  $\rho = 0.5, 12, 15, 20$ , and  $24.4$ . Where appropriate, we perform 2D computations on radial meshes on manifolds and refine the estimates for the quasipotential barriers between different basins or regions of the phase space.



### 5.1 $0 < \rho < 1$

For  $0 < \rho < 1$ , the origin is globally attracting. Two level sets of the quasipotential for  $\rho = 0.5$  are shown in Fig. 5. The computation was performed on  $513 \times 513 \times 513$  mesh with the update factor  $K = 14$ . This choice of  $K$  for  $N = 513$  was suggested in [31]. The level sets are heart-shaped and oriented approximately along the plane  $x_1 = x_2$ . Let  $X$  be a level set and let  $\gamma_X$  be the intersection of  $X$  with the vertical plane  $x_1 = x_2$ . The curve  $\gamma_X$  runs approximately along the edge of the heart-shaped level set  $X$ . We pick  $X$  to be a level set corresponding to one of the largest computed values of the quasipotential and find a collection of points marked with large orange dots lying on the corresponding curve  $\gamma_X$  and forming angles from 0 to  $2\pi$  with step  $\pi/72$ . The characteristics of (1) (the dark blue curves) and the MAPs of (2) (the dark red curves) starting and arriving at this set of points, respectively, are notably different. We also see that the set of characteristics starting at  $\gamma_X$  and the set of MAPs arriving at  $\gamma_X$  form visibly distinct 2D manifolds.

Let  $J$  be the Jacobian matrix of the right-hand side of (1) evaluated at the origin:

$$J = \begin{bmatrix} -\sigma & \sigma & 0 \\ \rho & -1 & 0 \\ 0 & 0 & -\beta \end{bmatrix}. \quad (24)$$

For the linear SDE

$$d\mathbf{x} = J\mathbf{x}dt + \sqrt{\epsilon}d\mathbf{w}, \quad (25)$$

the quasipotential decomposition is given by  $J\mathbf{x} = -Q\mathbf{x} + L\mathbf{x}$  (see Appendix A), where  $Q$  and  $L$  are matrices. The quasipotential is the quadratic form  $U(\mathbf{x}) = \mathbf{x}^\top Q\mathbf{x}$  where  $Q$  can be found analytically [4]:

$$Q = \begin{bmatrix} Q_1 & \\ & \beta \end{bmatrix}, \quad \text{where} \quad (26)$$

$$Q_1 = \frac{\sigma + 1}{d} \begin{bmatrix} \sigma(\sigma + 1) + \rho(\rho - \sigma) & -\rho - \sigma^2 \\ -\rho - \sigma^2 & (\sigma + 1) - \sigma(\rho - \sigma) \end{bmatrix}, \quad (27)$$

$$d = (\sigma + 1)^2 + (\rho + \sigma)^2.$$

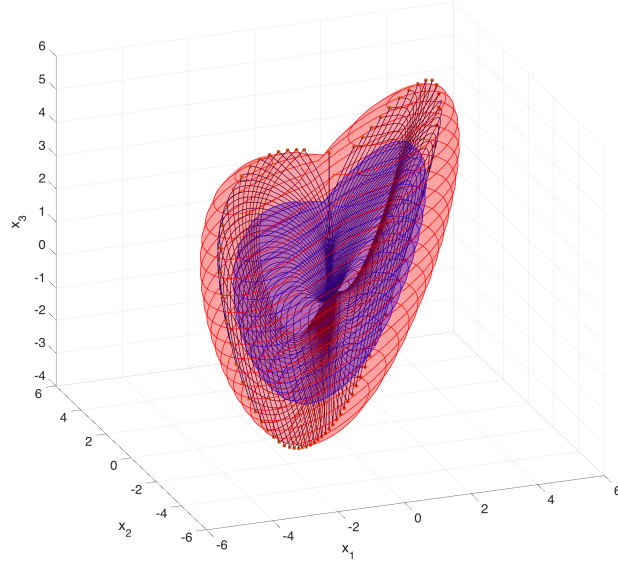
The rotational matrix  $L = J + Q$  is

$$L = \begin{bmatrix} L_1 & \\ & 0 \end{bmatrix}, \quad \text{where} \quad (28)$$

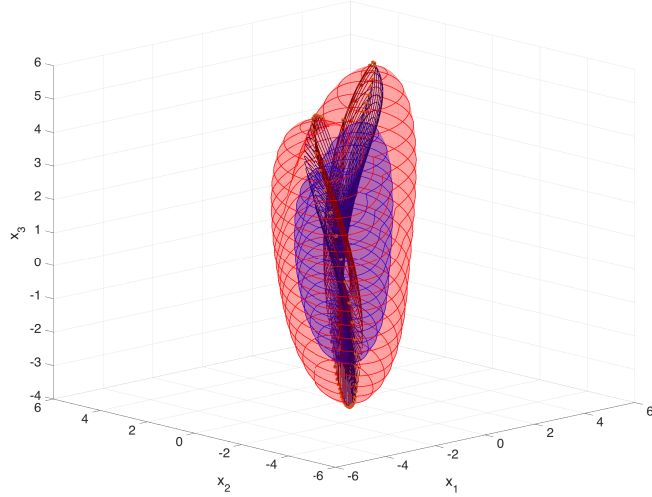
$$L_1 = \frac{\rho - \sigma}{d} \begin{bmatrix} \rho + \sigma^2 & -(\sigma + 1) + \sigma(\rho - \sigma) \\ \sigma(\sigma + 1) + \rho(\rho - \sigma) & -\rho - \sigma^2 \end{bmatrix}.$$

For the linear SDE (25), MAPs are the characteristics of  $\dot{\mathbf{x}} = (Q + L)\mathbf{x}$ . Obtaining spectral decompositions of  $J = -Q + L$  and  $\tilde{J} = Q + L$  for  $\rho = 0.5$  we find that typical characteristics of (1) approach the origin tangent to the line  $\text{span}(\mathbf{v})$ , while typical MAPs emanate from the origin tangent to the line  $\text{span}(\tilde{\mathbf{v}})$ , where

$$\mathbf{v} \approx \begin{bmatrix} 0.7241 \\ 0.6897 \\ 0 \end{bmatrix}, \quad \tilde{\mathbf{v}} \approx \begin{bmatrix} 0.6924 \\ 0.7215 \\ 0 \end{bmatrix}. \quad (29)$$



(a)



(b)

Figure 5: Two views of the level sets of the quasipotential at  $\rho = 0.5$  corresponding to  $U = 20$  (the blue surface) and  $U = 40$  (the red surface). Blue and red closed curves are shown to aid 3D visualization. The dark blue curves depict a collection of characteristics starting at the set of points marked by large orange dots and approaching the origin. The dark red curves represent a collection of the MAPs emanating from the origin and arriving at the same set of points. Click [here](#) to see a movie with this figure rotating around  $x_3$ -axis.

## 5.2 $1 < \rho < \rho_0 \approx 13.926$

In this interval, the equilibria  $C_{\pm}$  switch from stable nodes to stable spiral points at  $\rho \approx 2.1546$ . Fig. 6 displays the level sets of the quasi-potential for  $\rho = 12$  with respect to each stable equilibrium. It was computed on a  $513 \times 513 \times 513$  mesh with  $K = 14$ . The computed value of the quasipotential at the origin that serves as the transition state between  $C_{\pm}$  is 19.47. Therefore, at  $\rho = 12$ , the expected escape time from the basin of  $C_+$  scales as

$$\mathbb{E}[\tau_{C_+}] \asymp e^{19.47/\epsilon}. \quad (30)$$

The MAP from  $C_+$  to  $C_-$  is obtained by the concatenation of the computed MAP from  $C_+$  to the origin (the dark red curve starting at  $C_+$ ) and the characteristic from the origin to  $C_-$  (the dark blue curve ending at  $C_-$ ). Fig. 6(b) shows that the MAPs and the characteristics connecting  $C_{\pm}$  and the origin lie on close 2D manifolds.

## 5.3 $\rho_0 \approx 13.926 < \rho < \rho_1 \approx 24.06$

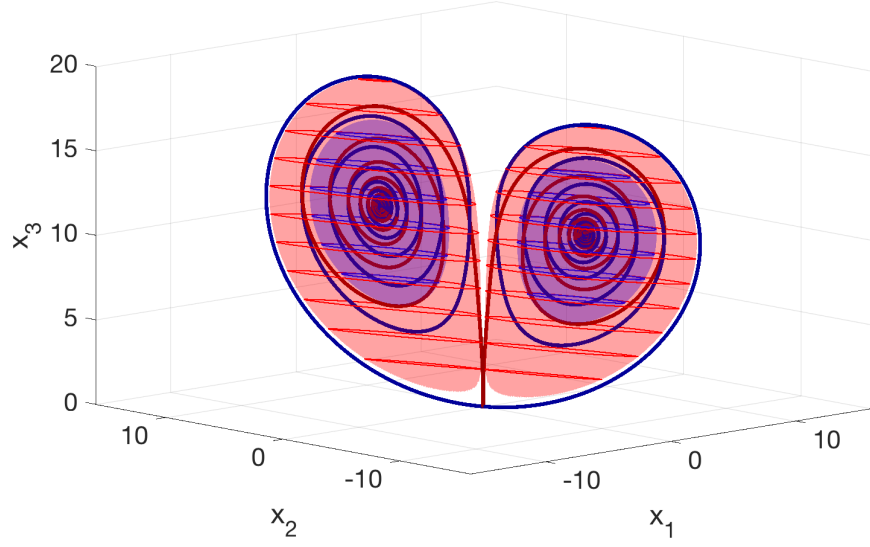
In this range, the escape states from  $C_+$  and  $C_-$  are the saddle limit cycles  $\gamma_+$  and  $\gamma_-$  respectively. We have computed the quasipotential for two values of  $\rho$ :  $\rho = 15$  and  $\rho = 20$ .

### 5.3.1 $\rho = 15$

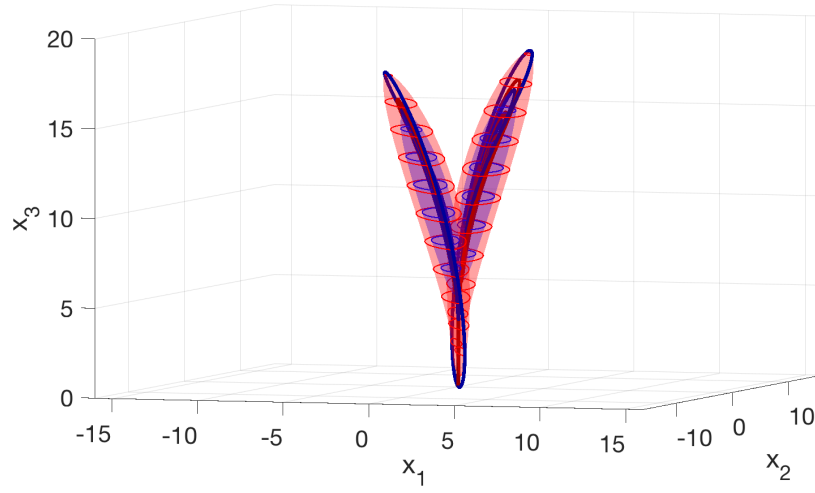
The computed quasipotential for  $\rho = 15$  with respect to  $C_+$  is visualized in Fig. 7. First, we picked a large computational domain to embrace the level set of the quasipotential enclosing both of the stable equilibria  $C_{\pm}$  and used a  $613 \times 613 \times 613$  mesh and  $K = 15$ . Second, we chose a smaller domain just to enclose  $\gamma_+$ . It was a cube with side 13 centered at  $C_+$ , and the mesh in it was  $1001 \times 1001 \times 1001$ .  $K$  was set to 20. The found quasipotential is nearly constant on  $\gamma_+$ : it varies between 17.42 and 17.45. The saddle cycles  $\gamma_{\pm}$  are depicted with thick bright red curves. A maximum likelihood transition path from  $C_+$  to  $C_-$  can be obtained by the concatenation of a MAP from  $C_+$  to  $\gamma_+$ , the saddle cycle  $\gamma_+$ , and a characteristic going from  $\gamma_+$  to  $C_-$ . One such a MAP and one such a characteristic are shown with the dark red and dark blue curves in Fig. 7 respectively.

Willing to refine our relatively rough 3D computation and find a more accurate value of the quasipotential on  $\gamma_+$  with respect to  $C_+$ , we perform 2D computations on the manifold  $\mathcal{M}_+$  consisting of all characteristics going from  $\gamma_+$  to  $C_+$ . Fig. 7 suggests that  $\mathcal{M}_+$  is close to the 2D manifold consisting of all MAPs from  $C_+$  to  $\gamma_+$ . So, we neglect the discrepancy between them. We generate 2D radial meshes on  $\mathcal{M}_+$  (see Appendix B) whose coarsened version is shown in Fig. 8(a). The computed quasipotential on  $\mathcal{M}_+$  is shown in Fig. 8(b). We first ran the OLIM on a radial mesh of size  $2001 \times 7200$  and then repeated the computation on a refined mesh of size  $4001 \times 14400$ . The radial update factors  $K_r$  were 50 and 100 respectively, and the angular update factors  $K_l$  were 180 and 360 respectively. For the coarser mesh, the resulting values of the quasipotential on  $\gamma_+$  varied from 18.19488 to 18.19501 averaging at 18.19495. For the finer mesh, these numbers were, respectively, 18.19536, 18.19541, and 18.19536. Hence, we obtain the following estimate for expected escape time from  $C_+$  at  $\rho = 15$ :

$$\mathbb{E}[\tau_{C_+}] \asymp e^{18.2/\epsilon}. \quad (31)$$

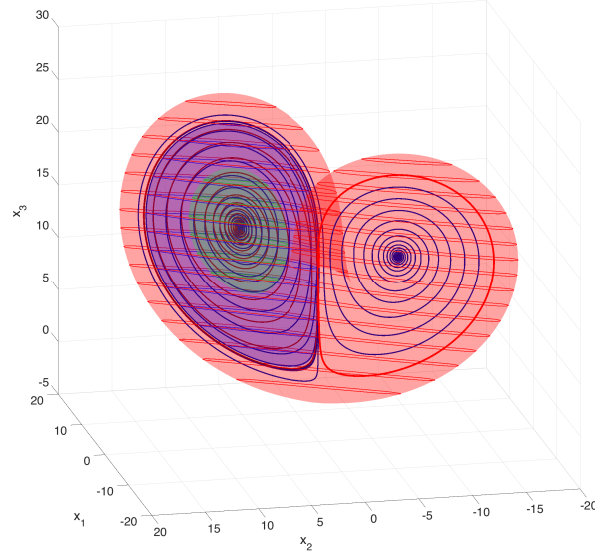


(a)

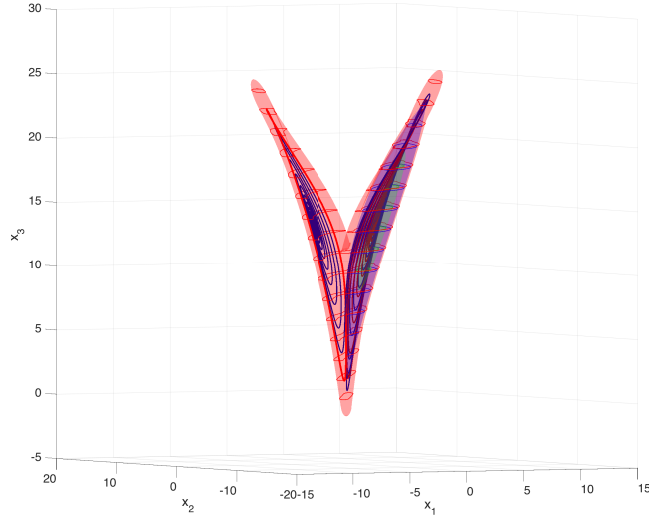


(b)

Figure 6: Two views of the level sets of the quasipotential at  $\rho = 12$  corresponding to  $U = 10$  (the blue surface) and  $U = 19.42$  (the red surface). The dark blue curves are the characteristics emanating from the origin along  $\pm\xi$  and arriving at  $C_{\pm}$  respectively. The dark red curves are the MAPs going from  $C_{\pm}$  to the origin. Click [here](#) to see a movie with this figure rotating around  $x_3$ -axis.



(a)



(b)

Figure 7: Two views of the level sets of the quasipotential at  $\rho = 15$  corresponding to  $U = 8$  (the green surface),  $U = 17.37$  (the blue surface), and  $U = 20$  (the red surface). The thick bright red curves are the saddle cycles  $\gamma_{\pm}$ . The dark blue curves are characteristics running from  $\gamma_+$  and approaching  $C_{\pm}$ . The dark red curve is a MAP starting at  $C_+$  and approaching  $\gamma_+$ . Click [here](#) to see a movie with this figure rotating around  $x_3$ -axis.

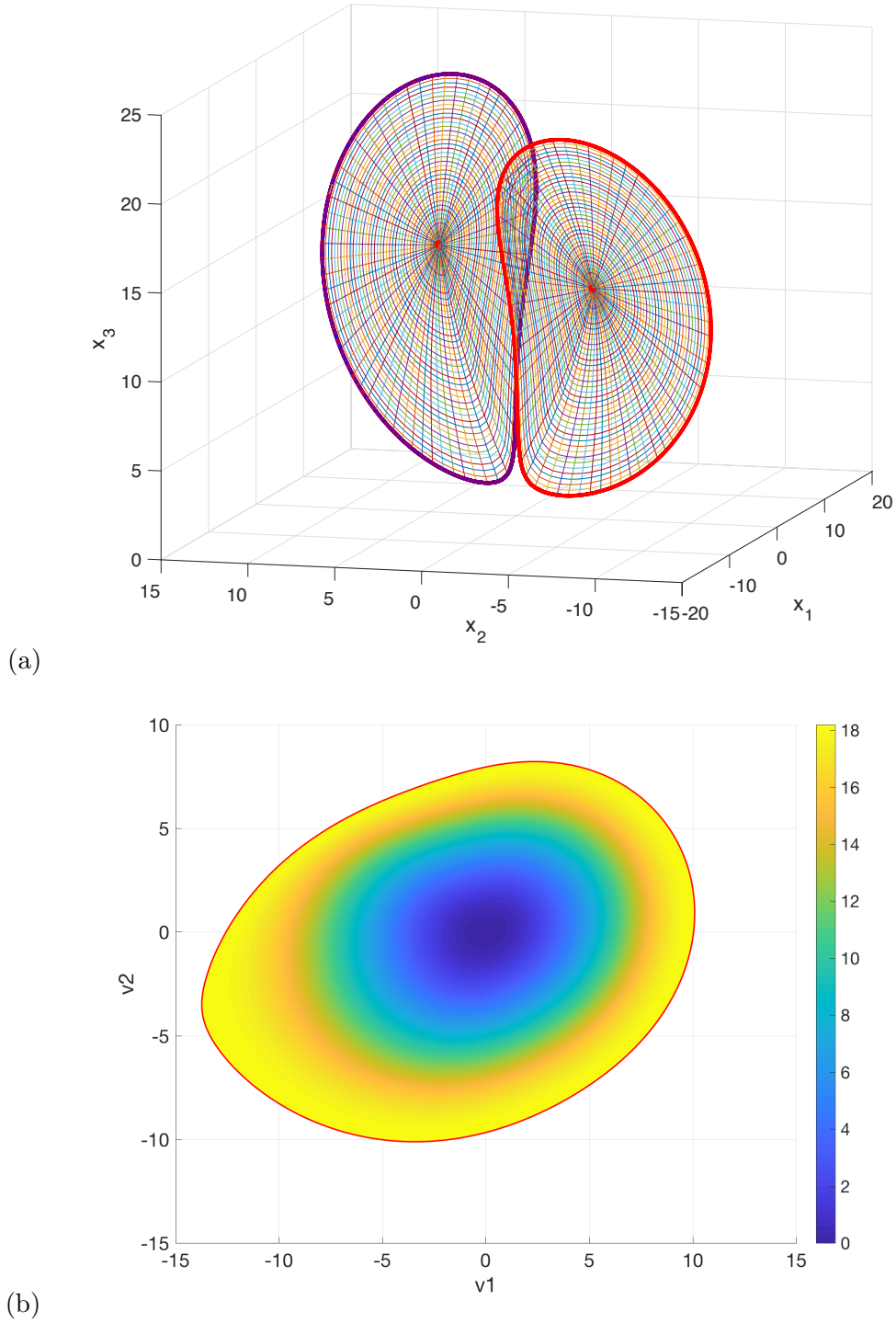


Figure 8: (a): Radial meshes on the manifold  $\mathcal{M}_\pm$  consisting of all characteristics going from the saddle cycles  $\gamma_+$  (the thick purple curve) and  $\gamma_-$  (the thick red curve) to the equilibria  $C_\pm$  (the large red dots) respectively. (b): The Quasipotential computed on  $\mathcal{M}_+$ .

### 5.3.2 $\rho = 20$

For  $\rho = 20$ , we performed a computation in the cube with side 26 centered at  $C_+$  on a  $1001 \times 1001 \times 1001$  mesh with  $K = 20$ . This cube encloses  $\gamma_+$ . The values of the computed quasipotential on  $\gamma_+$  range from 6.59 to 6.62 and average at 6.61. The level sets corresponding to  $U = 3.3$  and  $U = 6.58$  are shown in Fig. 9. A 2D computation on the manifold  $\mathcal{M}_+$  similar to the one described in Section 5.3.1 gave  $U(\gamma_+) \in [6.1172, 6.1175]$  with the average at 6.1172. The MAP going from  $C_+$  to  $\gamma_+$  as well as the characteristics going from  $\gamma_+$  to  $C_+$  spiral notably denser than their counterparts at  $\rho = 15$ , and the level sets of the quasipotential are thinner. Speaking informally, the saddle cycles are the escape states from the basins of  $C_\pm$  to a “joker” region [20] where it is hard to predict for a characteristic which attractor,  $C_+$  or  $C_-$ , it will eventually approach. We traced 1000 trajectories starting on the cone  $\Upsilon_+$  at the points of the form  $\mathbf{y}_i := \mathbf{x}_i + 0.002(\mathbf{x}_i - C_+)$  where  $\mathbf{x}_i \in \gamma_+$ ,  $i = 1, \dots, 1000$ , are equispaced, and recorded whether they converged to  $C_+$  or  $C_-$  as  $t \rightarrow \infty$ . Then we subdivided  $\gamma_+$  into 100 intervals of equal length and used the recorded data to estimate the probability for a trajectory starting at each  $\mathbf{y}_i$  corresponding to  $\mathbf{x}_i$  in each interval to converge to  $C_+$ . The result is shown in Fig. 10(a). The probabilities for  $\gamma_-$  are obtained by symmetry. Summarizing our findings for  $\rho = 20$ , we predict that the expected escape time from  $C_\pm$  to the joker region scales as

$$\mathbb{E}[\tau_{C_+}] \asymp e^{6.1/\epsilon}. \quad (32)$$

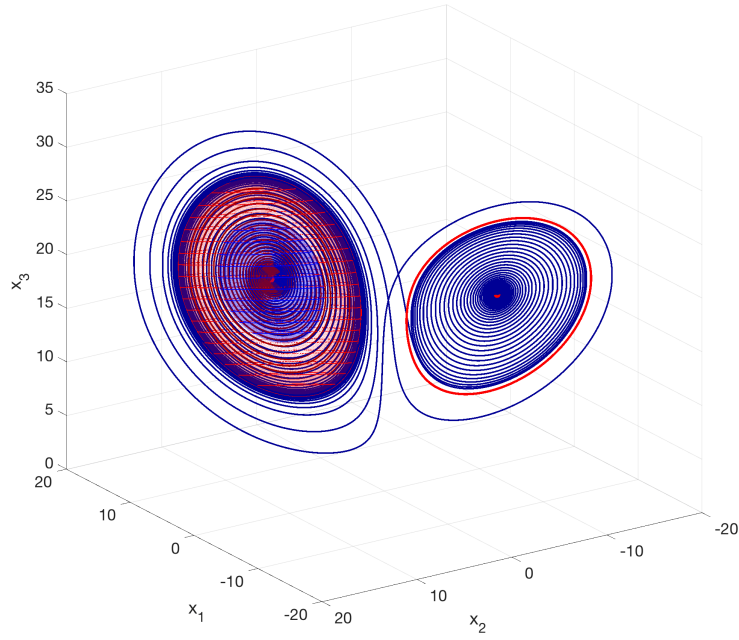
Note that a similar calculation for  $\rho = 15$  gave the probability distribution depicted in Fig. 10(b): 975 out of 1000 trajectories starting at the analogous points of the cone  $\Upsilon_+$  eventually approached  $C_-$ , while 25 returned to  $C_+$ .

### 5.4 $\rho_1 \approx 24.06 < \rho < \rho_2 \approx 24.74$

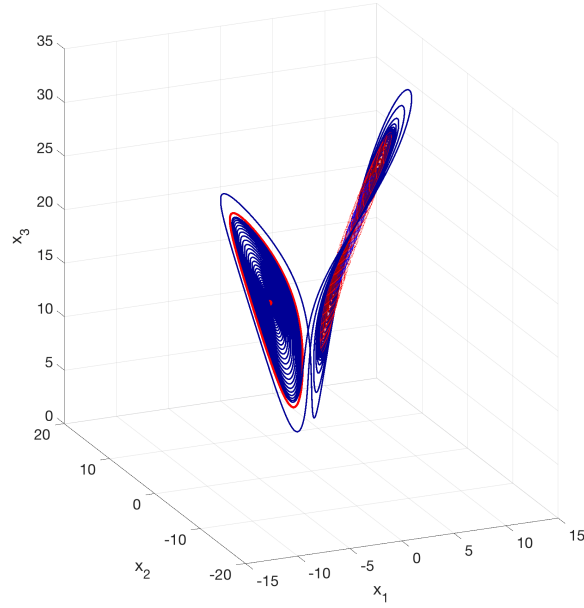
It was recognized by Lorenz [19] that the strange attractor is an “infinite complex of surfaces”, i.e., a fractal, which is a very complicated geometric object. The addition of small white noise to the Lorenz system regularizes and simplifies its dynamics in the sense that it renders the fine structure of the Lorenz attractor irrelevant and allows for a description of the dynamics in terms of probability measures. Taking this into account, we approximate the strange attractor  $A_L$  with a union of four manifolds as shown in Fig. 11. We will refer to the inner boundaries of the red and blue manifolds plotted with brown and cyan, respectively, as the eyes  $Y_+$  and  $Y_-$ . The union of the red and green boundaries will be called wing  $W_+$ . Similarly, the union of the blue and magenta boundaries forms the wing  $W_-$ . In order to understand what is the minimal reasonable value of the parameter  $\epsilon$  in (2) that makes such an approximation sensible, we estimated thickness of the strange attractor at 398 randomly picked points. Details are provided in Appendix B. The thickness map in Fig. 11 indicates that the thickness of  $A_L$  does not exceed  $10^{-2}$  wherever it is approximated by a single manifold. Larger values of thickness are found in places where we approximate  $A_L$  with two close manifolds. The thickness map suggests that  $\sqrt{\epsilon}$  in SDE (2) should be at least  $10^{-2}$ , i.e.,  $\epsilon \gtrsim 10^{-4}$ .

We performed a 3D computation of the quasipotential aiming at obtaining the overall picture. The computational domain was a box centered at  $C_+$  and embracing the strange attractor. Note that this computation is too rough to give accurate numbers, nevertheless, it captures the geometry of the level sets. The level sets of the computed quasipotential shown in Fig. 12 agree with our expectations: the quasipotential grows until it reaches the strange attractor, it remains nearly constant near it, and then growth fast away from it. Again, we performed a 2D computation on the manifold  $\mathcal{M}_+$  on a radial  $6001 \times 7200$  mesh with  $K_r = 150$  and  $K_a = 500$  and found the quasipotential at  $\gamma_+$  to be equal to 0.03466 (see Fig. 13).





(a)



(b)

Figure 9: Two views of the level sets of the quasipotential at  $\rho = 20$  corresponding to  $U = 3.3$  (the blue surface), and  $U = 6.58$  (the red surface). The thick bright red curves are the saddle cycles  $\gamma_{\pm}$ . The dark blue curves are characteristics going from  $\gamma_{+}$  to  $C_{+}$  and  $C_{-}$ . The dark red curve is a MAP starting at  $C_{+}$  and approaching  $\gamma_{+}$ . Click [here](#) to see a movie with this figure rotating around  $x_3$ -axis.

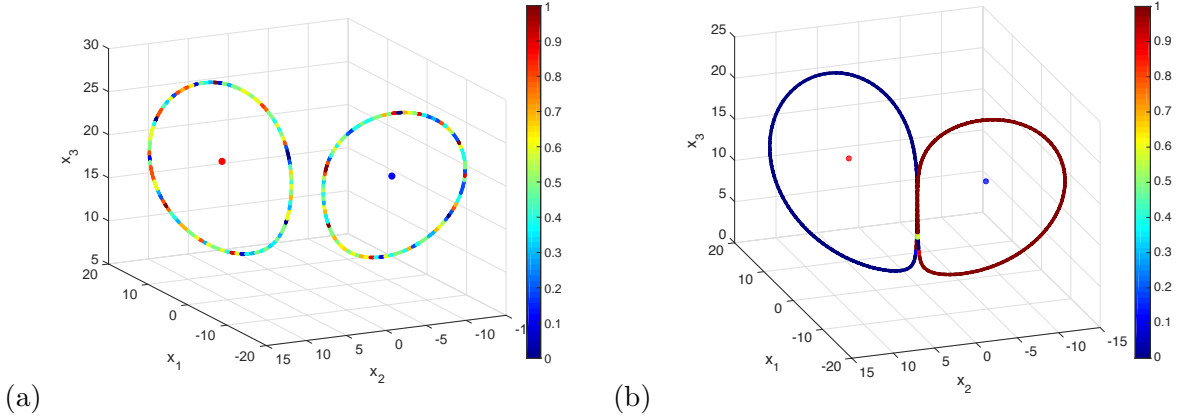


Figure 10: The probability for a trajectory starting on the cones  $\Upsilon_{\pm}$  at the point of the form  $\mathbf{x} + 0.002(\mathbf{x} - C_{\pm})$  where  $\mathbf{x} \in \gamma_{\pm}$  respectively to converge to  $C_+$ . (a):  $\rho = 20$ . (b):  $\rho = 15$ .

Looking at Fig. 11, we spot two possible transition mechanisms from the strange attractor to  $C_+$ . The first one would start near the eye  $Y_+$ , climb up to  $\gamma_+$ , and then switch to spiraling toward  $C_+$ . The second one would involve sliding toward  $\gamma_+$  from the neighborhood of the wing  $W_-$  to a region lying between the eye and  $\gamma_+$  and starting spiraling toward  $\gamma_+$  and then toward  $C_+$ . Coarsened versions of meshes generated for computing the quasipotential barriers for each of these transition mechanisms are displayed in Fig. 14 (a) and (c) respectively. The “eye” mesh in Fig. 14(a) is lying on the unstable loop-shaped manifold of  $\gamma_+$  between the  $\gamma_+$  and  $Y_+$ . Its size is  $1501 \times 6000$ . The found quasipotential on  $\gamma_+$  is 0.01543 (see Fig. 14(b)). The “wing+eye” mesh in Fig. 14(c) is defined on the union of the following two manifolds. The wing manifold is defined by trajectories starting near the negative  $x_3$ -semiaxis and bounded by  $W_+$  and a trajectory approaching  $\gamma_+$ . The second one is the loop-shaped unstable manifold of  $\gamma_+$  located between  $\gamma_+$  and  $Y_+$ . The total mesh size is  $1501 \times 26001$  whose  $1501 \times 6000$  piece covers the loop. The quasipotential computed on it is shown in Fig. 14(d). Its part corresponding to the loop, naturally, involves significantly smaller values than the one corresponding to the strip around the wing. The quasipotential value on  $\gamma_+$  for this mesh is 0.01479 which is smaller than the one for the eye mesh.

As we have mentioned above, the strange attractor has a finite width varying roughly from 0 to  $10^{-2}$ . This means that, in order to treat it as a union of four manifolds as shown in Fig. 11 while considering the dynamics according to SDE (2), the parameter  $\epsilon$  should be chosen at least as large as  $10^{-4}$ . The discussed transition mechanisms from  $A_L$  to  $C_{\pm}$  are associated with close quasipotential barriers: the difference between them is about  $5 \cdot 10^{-4}$ . Therefore, in order to determine which transition mechanism is dominant for  $\epsilon \sim 10^{-4}$ , one needs to compute the pre-exponential factors of the corresponding transition rates. Estimation of these prefactors is beyond the scope of the present work. We leave the development of numerical methods for their evaluation for the future.

## 5.5 Perspectives and challenges for large $\rho$

Our numerical experiments show that the level sets of the quasipotential thin out as  $\rho$  grows. On one hand, this creates numerical challenges for 3D computations of the quasipotential as mesh planes are, in general, not aligned with its level sets. Moreover, the diameter of the strange attractor or stable limit cycles appearing at certain intervals of  $\rho$  also increases as  $\rho$  grows (Fig. 1) requiring larger

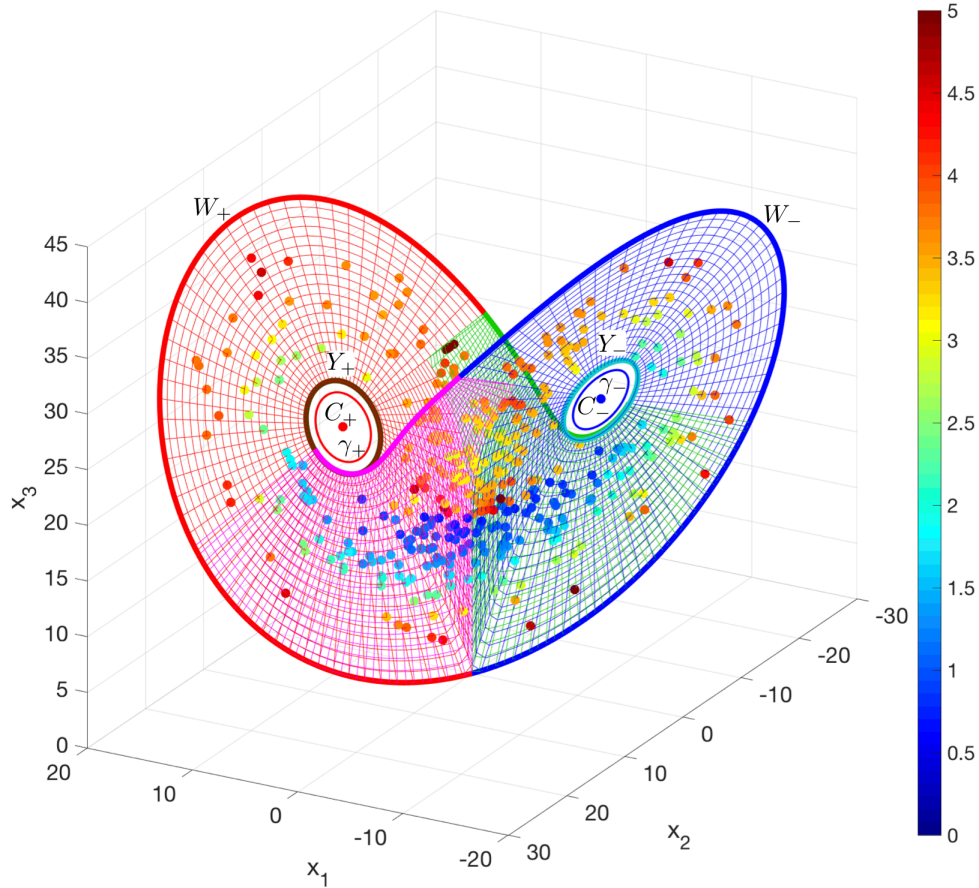
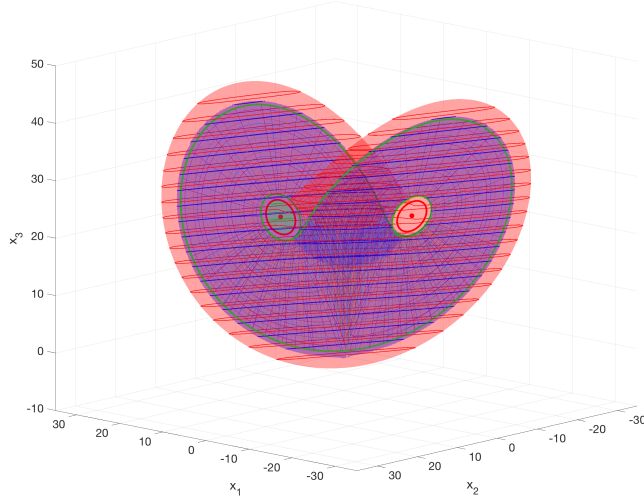
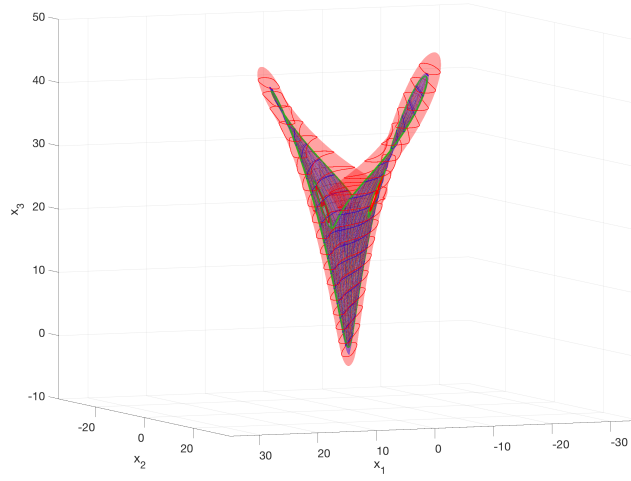


Figure 11: The strange attractor  $A_L$  at  $\rho = 24.4$  by a union of four manifolds: red, magenta, blue, and green. The color of the large dots on the manifolds indicate the thickness of the fractal (the Lorenz attractor) at the corresponding locations. The colorbar corresponds to  $-\log_{10} w(\mathbf{x})$  where  $w(\mathbf{x})$  is the thickness of the fractal near the location  $\mathbf{x}$ . Hence dark blue dots indicate thickness  $\sim 10^{-1}$ , light blue ones  $\sim 10^{-2}$ , green ones  $\sim 10^{-3}$ , orange ones  $\sim 10^{-4}$ , and red ones  $\sim 10^{-5}$ .



(a)



(b)

Figure 12:  $\rho = 24.4$ . Two views of the level sets of the quasipotential computed with respect to  $C_+$ . The green surface corresponds to the quasipotential value slightly less than the one at  $\gamma_+$ . The blue and red ones correspond to  $U = 2$  and  $U = 20$  respectively. The strange attractor is depicted with a mesh visible inside the blue and red surfaces. Click [here](#) to see a movie with this figure rotating around  $x_3$ -axis.

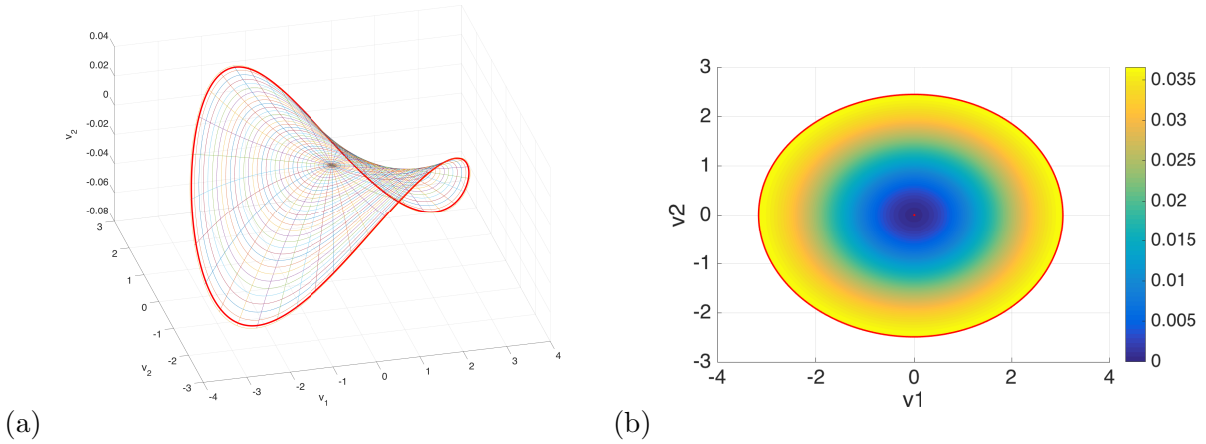


Figure 13: (a): A coarsened radial mesh on the manifold  $\mathcal{M}_+$  at  $\rho = 24.4$ . The coordinate system is associated with the directions of eigenvectors of the quasipotential matrix for the Jacobian evaluated at  $C_+$ . (b): The quasipotential computed on this mesh.

and larger computational domains. Handling this issue by means of mesh refinement combined with enlarging the box serving as a computational domain is limited by computer's memory. On the other hand, thinning out of the level sets allows us to use 2D computations provided that we have an insight about possible transition mechanisms as we have had for  $\rho = 24.4$ .

As one can see from Fig. 1, at certain intervals of values of  $\rho > 24.74$ , Lorenz system admits pairs of attracting limit cycles. For example, two symmetric limit cycles exist at  $\rho = 100.75$ . A question of interest would be the one of finding the quasipotential barrier between them. We leave this computation for the future because it would require the further enhancement of 3D quasipotential solvers as the level sets of the quasipotential at  $\rho = 100.75$  are too thin for the current version.

## 6 Conclusions

We have demonstrated an application of the recently developed 3D quasipotential solver based on the ordered line integral method (OLIM) with the midpoint quadrature rule to the Lorenz'63 system perturbed by small white noise (2). Our 3D computations have been done for the parameter values  $\sigma = 10$ ,  $\beta = 8/3$ , and a number of values of  $\rho$  ranging from 0.5 to 24.4. As  $\rho$  increases, the level sets of the quasipotential thin out and the magnitude of the rotational component grows dramatically in comparison with that of the potential component. On one hand, these facts render the numbers produced by 3D computations less accurate. On the other hand, the manifolds consisting of characteristics going from escape states to attractors and those consisting of MAPs running from the other way around become very close to each other. This observation motivated us to approximate the latter manifolds with the former ones.

Hence, we have developed a technique for generating radial meshes on manifolds consisting of such characteristics. We have tested our 2D OLIM quasipotential solver on an ad hoc system where the magnitude of the rotational component exceeds that of the potential one by the factor at least as large as  $10^3$ , approximately as it is for  $\rho = 24.4$  in (2). The test results on radial meshes  $N_r \times N_a$  where  $N_a = 2N_r$  with the update factors  $K_r = \text{round}(N_r/40)$  and  $K_a = 2K_r$  have shown a

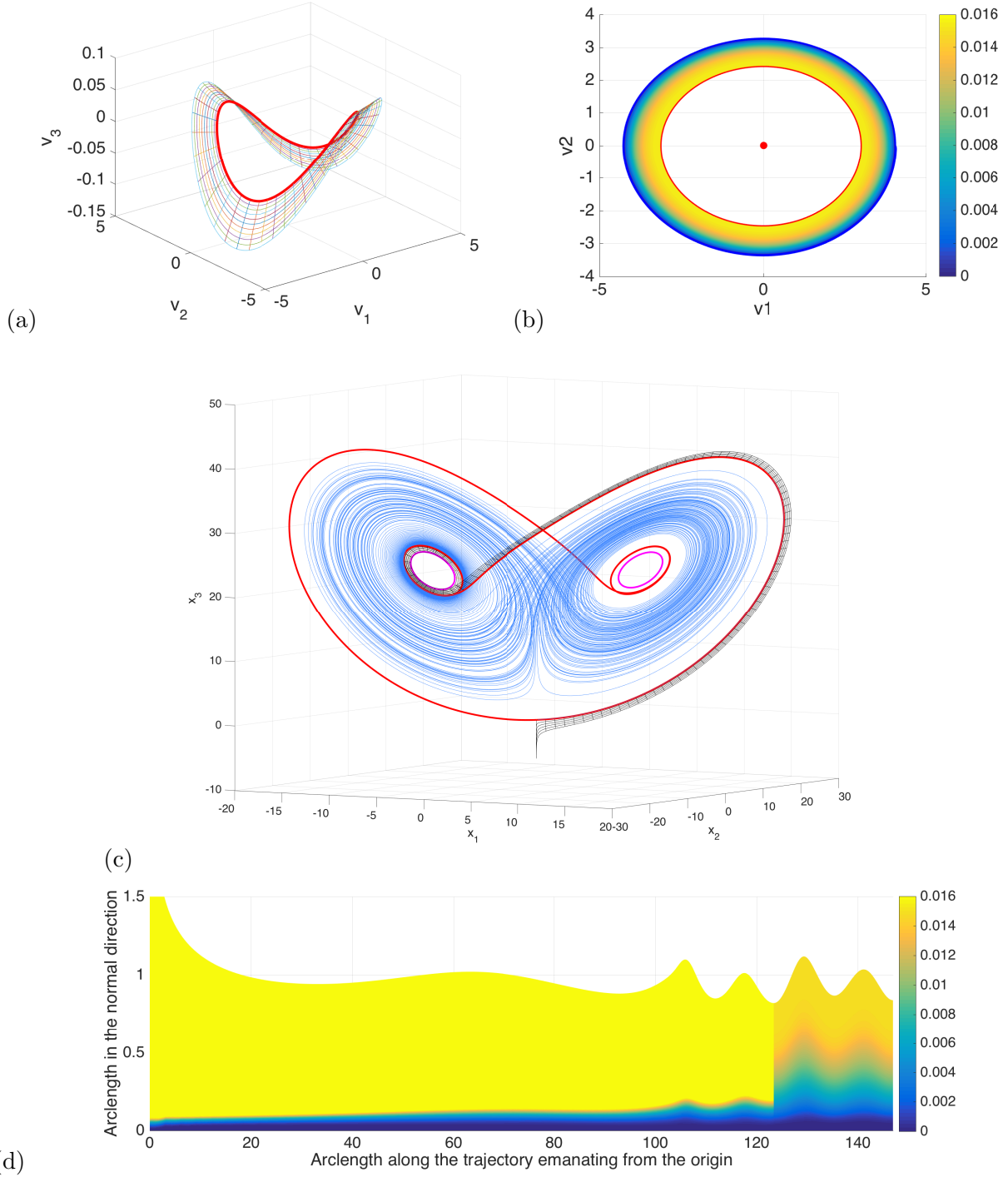


Figure 14:  $\rho = 24.4$ . (a): A coarsened version of the “eye” mesh. The coordinate axes  $\mathbf{v}_i$ ,  $i = 1, 2, 3$  are chosen along the eigenvectors of the quasipotential matrix  $Q$  of the linearized near  $C_+$  vector field. (b): the quasipotential computed on the “eye” mesh. (c): A coarsened version of the “wing+eye” mesh. (d): The quasipotential computed on the “wing+eye” mesh.

superquadratic convergence and small normalized maximal absolute errors on practical mesh sizes.

Using a combination of 3D and 2D computations, we found quasipotential barriers necessary to overcome in order to escape from the basins of from  $C_{\pm}$  at  $\rho = 12, 15, 20$ , and  $24.4$ . Furthermore, we estimated quasipotential barriers for escaping from the basin of the strange attractor at  $\rho = 24.4$  via two escape mechanisms. These barriers for  $24.4$  are close to each other: the difference between them is of the same order of magnitude as the minimal value of  $\epsilon$  that makes traversing between different sheets of the Lorenz attractor easy. Therefore, estimates for pre-exponential factors for escape rates are necessary in order to determine which transition mechanism is dominant. We have left the development of techniques for computing these prefactors for the future.

Another important advantage of computing the quasipotential in 3D is that it allows us to visualize the stochastic dynamics. Plots of quasipotential level sets reveal the hierarchy of regions of the phase space reachable by the system perturbed by small white noise on different timescales. In particular, the visualization of the level sets of the quasipotential at  $\rho = 24.4$  suggested us to consider and compare two possible transition mechanisms between the strange attractor and the stable equilibria.

Our C and Matlab programs developed for the application to Lorenz'63 are packaged into `Qpot4Lorenz63.zip` and posted on M. Cameron's web site [5].

The application to the Lorenz'63 model allows us to see the limitations of the 3D quasipotential solver: the growth of required computational domains together with thinning out of the level sets results in underresolving the latter even with the use of  $1001^3$  mesh sizes. On the other hand, it motivates the directions of the future research associated with (i) combining the 3D OLIMs with techniques for generating of 3D mesh adapted for the geometry of the problem and (ii) advancing of the techniques for learning 2D manifolds near which the stochastic dynamics is effectively focused.

## Acknowledgements

We thank Dr. E. S. Kurkina for inspiring discussions on the Lorenz'63 system and sharing numerical techniques for plotting bifurcational diagrams and finding unstable limit cycles. This work is partially supported by the NSF grant DMS1554907.

## A Quasipotential decomposition for linear SDEs

In this Appendix, we explain how one can find the quasipotential for linear SDEs for which the origin is an asymptotically stable equilibrium. This is useful for initializing the OLIMs near asymptotically stable equilibria and for estimating the ratio of the magnitudes of the rotational and potential components of the vector field.

Let  $J$  be a  $d \times d$  matrix with all eigenvalues having negative real parts. In this work,  $J$  is the Jacobian matrix of the vector field  $\mathbf{b}$  evaluated at an asymptotically stable equilibrium  $\mathbf{x}^*$  of  $\dot{\mathbf{x}} = \mathbf{b}(\mathbf{x})$ . We consider the linear SDE for the variable  $\mathbf{y} := \mathbf{x} - \mathbf{x}^*$ :

$$d\mathbf{y} = J\mathbf{y}dt + \sqrt{\epsilon}d\mathbf{w}. \quad (33)$$

The problem of finding the quasipotential decomposition for the vector field  $J\mathbf{y}$  reduces to the problem of finding a symmetric positive definite matrix  $Q$  such that [6, 7]

$$\mathbf{y}^\top Q(J + Q)\mathbf{y} = 0 \quad \text{for all } \mathbf{y} \in \mathbb{R}^d. \quad (34)$$



The matrices  $Q$  and  $L := J + Q$  are called the *quasipotential matrix* and the *rotational matrix* respectively. Condition (34) is equivalent to the requirement that the matrix  $Q(J + Q)$  is antisymmetric, i.e.,  $Q(J + Q) + (J + Q)^\top Q = 0$ . The last equation for  $Q$  is reducible to a Sylvester equation for  $Q^{-1}$  and has a unique positive definite solution that can be found using the Bartels-Stewart algorithm implemented in Matlab in the command `sylvester` (see [31]) for details).

To make our quasipotential solver for the Lorenz system self-contained and facilitate experiments with various values of  $\rho$ , we have developed a C code `LinLorenz.c` for finding the quasipotential decomposition for the Lorenz system linearized near its asymptotically stable equilibria. The quasipotential decomposition is found by an algorithm similar to Bartels-Stewart but simplified and customized for Lorenz'63. A description of it is linked to the provided software package [5].

Once the quasipotential decomposition for a linearized system is available, one can obtain an estimate for the ratio  $\Xi(\mathbf{x})$  of the magnitudes of the rotational and the potential components near asymptotically stable equilibria:

$$\Xi \lesssim \max_{\|\mathbf{y}\|=1} \frac{\|L\mathbf{y}\|}{\|Q\mathbf{y}\|}. \quad (35)$$

The graph of the right-hand side of (35) with  $J$  been the Jacobian matrix evaluated at  $C_+$  of (1) is plotted Fig. 3 for the range  $1 < \rho < \rho_2 \approx 24.74$ .

## B Building radial meshes

Suppose we would like to build a radial mesh on a 2D manifold formed by characteristics of  $\dot{\mathbf{x}} = \mathbf{b}(\mathbf{x})$  going from an unstable limit cycle  $\gamma$  to an asymptotically stable spiral point  $\mathbf{x}^*$ . First, we pick a set of points  $\mathbf{x}^k$ ,  $k = 0, 1, \dots, N_a - 1$ , equispaced along  $\gamma$ . For each point  $\mathbf{x}^k$ , we define a plane  $\alpha^k$  passing through  $\mathbf{x}^*$  and  $\mathbf{x}^k$  whose normal  $\mathbf{a}^k$  lies in the plane spanned by  $\mathbf{b}(\mathbf{x}^k)$  and  $\mathbf{x}^k - \mathbf{x}^*$ .

Then, we trace a trajectory  $\mathbf{y}(t)$  starting near  $\gamma$  and ending upon reaching an  $\delta$ -ball centered at  $\mathbf{x}^*$  where  $\delta$  is a small number. Let  $\mathbf{y}_1, \dots, \mathbf{y}_n$  be the set of intersects of  $\mathbf{y}(t)$  with the plane  $\alpha^0$  at which the sign of  $(\mathbf{y}(t) - \mathbf{x}^0)^\top \mathbf{a}^0$  changes from “−” to “+”. Adding  $\mathbf{x}^0$  and  $\mathbf{x}^*$  to this set and interpolating, we get a curve lying in  $\alpha_0$  and connecting  $\gamma$  and  $\mathbf{x}^*$ . We define a set of points  $\{\mathbf{z}_i^0\}_{i=0}^{N_r-1}$  uniformly distributed along this curve such that  $\mathbf{z}_0^0 \equiv \mathbf{x}^*$  and  $\mathbf{z}_{N_r-1}^0 \equiv \mathbf{x}^0$ .

Next, for  $k = 0, 1, 2, \dots, N_a - 2$ , we trace the trajectories starting at  $\mathbf{z}_i^k$ ,  $i = 1, \dots, N_r - 2$ , and terminate them as soon as they reach the plane  $\alpha_{k+1}$ . As above, we add  $\mathbf{x}_{k+1}$  and  $\mathbf{x}^*$  to these terminal points, interpolate them, and pick a set of points  $\mathbf{z}_i^{k+1}$ ,  $i = 0, \dots, N_r - 1$ , uniformly distributed along the interpolant and such that  $\mathbf{z}_0^{k+1} \equiv \mathbf{x}^*$  and  $\mathbf{z}_{N_r-1}^{k+1} \equiv \mathbf{x}^{k+1}$ . As a result, we obtain the radial mesh

$$\{\mathbf{z}_i^k \mid 0 \leq i \leq N_r - 1, 0 \leq k \leq N_a - 1\}.$$

This procedure is implemented in the Matlab code `make2Dmesh.m` in `Qpot4Lorenz63.zip` [5].

Similar methodology has been used to construct radial meshes between two simple closed curves and between two given segments of two distinct characteristics.

## C Estimating the width of the Lorenz attractor

Let  $\mathbf{x}$  be a point lying on the Lorenz attractor  $A_L$  and let  $\alpha$  be the plane passing through  $\mathbf{x}$  and normal to  $\mathbf{b}(\mathbf{x})$  where  $\mathbf{b}$  is the Lorenz vector field, i.e.,

$$\alpha := \{\mathbf{z} \in \mathbb{R}^3 \mid (\mathbf{z} - \mathbf{x})^\top \mathbf{b}(\mathbf{x}) = 0\}.$$

We trace a trajectory  $\mathbf{y}(t)$  starting at  $\mathbf{x}$  for time  $10^4$  and record the points  $\mathbf{y}_i$ ,  $1 \leq i \leq N$  at which the sign of  $(\mathbf{y}(t) - \mathbf{x})^\top \mathbf{b}(\mathbf{x})$  switches from “−” to “+”. We set up a Cartesian coordinate system  $(\eta_1, \eta_2)$  in the plane  $\alpha$  with the origin at  $\mathbf{y}_1 \equiv \mathbf{x}$  and find the coordinates of the recorded points  $\mathbf{y}_i$ :  $\mathbf{y}_i \equiv (\eta_1^i, \eta_2^i)$ . We pick a square  $S := [-0.25 \leq \eta_1 \leq 0.25] \times [-0.25 \leq \eta_2 \leq 0.25]$  in this plane and select the subset  $I \subset \{1, \dots, N\}$  such that the points  $\mathbf{y}_i$ ,  $i \in I$ , lie in  $S$ . Visualizing the set  $\mathbf{y}_i$ ,  $i \in I$ , and zooming in if necessary, we see that they are arranged near two almost parallel lines (see Fig. 15). The least squares fit to this set of points with a linear function  $\eta_2 = a\eta_1 + b$  gives a line dividing it into two subsets:

$$I_1 = \{i \in I \mid \eta_2^i < a\eta_1^i + b\} \quad \text{and} \\ I_2 = \{i \in I \mid \eta_2^i > a\eta_1^i + b\}.$$

Next, we find linear least squares fits  $\eta_2 = a_1\eta_1 + b_1$  and  $\eta_2 = a_2\eta_1 + b_2$  for the subsets of  $\mathbf{y}_i$  corresponding to  $I_1$  and  $I_2$ , respectively. One of these linear functions must pass very close to the origin because  $\mathbf{x}$  lies near one of these lines, hence either  $b_1$  or  $b_2$  is very close to zero in comparison with the other one. Assume that  $|b_2| \ll |b_1|$ . If this is the other way around, we swap the notations. Also, these lines are almost parallel, hence  $a_1$  and  $a_2$  are very close. Finally, we find a line orthogonal to  $\eta_2 = a_1\eta_1 + b_1$  and passing through the origin:  $\eta_2 = -a_1^{-1}\eta_1$ . Then the thickness of  $A_L$  near  $\mathbf{x}$  is approximately equal to the distance between the origin and the intersect of  $\eta_2 = -a_1^{-1}\eta_1$  and  $\eta_2 = a_1\eta_1 + b_1$ . This technique is implemented in the Matlab program `thickness.m` in `Qpot4Lorenz63.zip` [5].

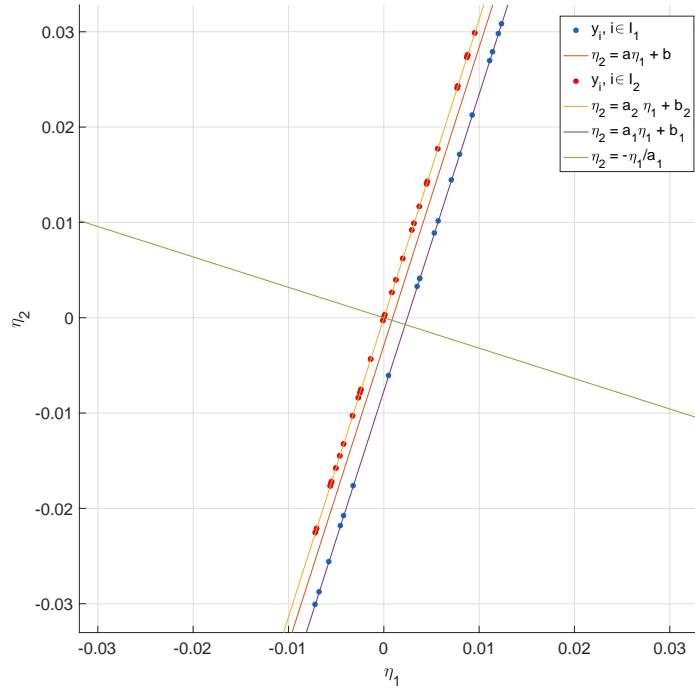


Figure 15: Estimating thickness of the Lorenz attractor using linear least squares fits in a Poincare section.

## References

- [1] R. Bartels and G. W. Stewart, *Solution of the matrix equation  $AX + XB = C$* , Comm A.C.M., 15 (1972), 9, 820–826
- [2] R. E. Bellman, *Dynamic Programming*, Princeton University Press, Princeton, NJ, 1957
- [3] F. Bouchet and J. Reygner, *Generalisation of the Eyring-Kramers Transition Rate Formula to Irreversible Diffusion Processes*, Annales Henri Poincare, 17 (2016), 12, pp. 3499–3532
- [4] M. K. Cameron, *Finding the Quasipotential for Nongradient SDEs*, Physica D: Nonlinear Phenomena, 241 (2012), pp. 1532–1550
- [5] <https://www.math.umd.edu/~mariakc/software-and-datasets.html>
- [6] Z. Chen, M. Freidlin, *Smoluchowski-Kramers approximation and exit problems*, Stoch. Dyn. 5 (2005), 4, pp. 569–585
- [7] Z. Chen, *Asymptotic Problems related to Smoluchowski-Kramers approximation*, Ph.D. Dissertation, UMD, 2006 <https://drum.lib.umd.edu/bitstream/handle/1903/3791/umi-umd-3634.pdf?sequence=1>
- [8] M. G. Crandall, P. L. Lions, *Viscosity solutions of Hamilton-Jacobi-Bellman equations*, Trans. Amer. Math. Soc. 277 (1983), pp. 1–43
- [9] D. Dahiya and M. Cameron, *Ordered Line Integral Methods for Computing the Quasi-potential*, J. Sci. Comput. (2017), (2017). <https://doi.org/10.1007/s10915-017-0590-9>
- [10] D. Dahiya and M. Cameron, *An Ordered Line Integral Method for Computing the Quasi-potential in the case of Variable Anisotropic Diffusion*, Physica D (2018) to appear, <https://doi.org/10.1016/j.physd.2018.07.002>, arXiv:1806.05321
- [11] S. V. Dudul, *Prediction of a Lorenz chaotic attractor using two-layer perceptron neural network*, Appl. Soft Computing 5 (2005), 333–355
- [12] J. Guckenheimer and R. F. Williams, *Structural stability of Lorenz attractors*, Publications Mathematiques, I.H.E.S. 50 (1980) 73–100
- [13] F. Hamilton, T. Berry, and T. Sauer, *Predicting chaotic time series with a partial model*, Phys. Rev. E 92 (2015) 010902(R)
- [14] M. I. Freidlin and A. D. Wentzell, *Random Perturbations of Dynamical Systems*, 3rd Ed, Springer-Verlag, Berlin Heidelberg, 2012.
- [15] M. Heymann, E. Vanden-Eijnden, *Pathways of maximum likelihood for rare events in non-equilibrium systems, application to nucleation in the presence of shear*, Phys. Rev. Lett. **100**, 14, 140601 (2007)
- [16] M. Heymann, E. Vanden-Eijnden, *The geometric minimum action method: a least action principle on the space of curves*, Comm. Pure Appl. Math. **61**, 8, 1052–1117 (2008)
- [17] H. Ishii, *A simple direct proof of uniqueness for solutions of the Hamilton-Jacobi equations of eikonal type*, Proc. Amer. Math. Soc. 100 (1987), 2, pp. 247–251

- [18] J. L. Kaplan and J. A. Yorke, Preturbulence: A Regime Observed in a Fluid Flow Model of Lorenz, *Commun. Math. Phys.* 67 (1979), 93–108
- [19] E. N. Lorenz, *Deterministic Nonperiodic Flow*, *J. Atmospheric Sci.*, 20 (1963), 2 pp. 130–141
- [20] G. G. Malinetskii, A. B. Potapov, *Channels and Jokers. New Approaches for Predicting Complex Dynamics*, Keldysh Institute preprints, 1998
- [21] D. Rand, The topological classification of Lorenz attractors, *Math. Proc. Camb. Phil. Soc.* 83 (1978) 451–460
- [22] B. Saltzman, Finite amplitude free convection as an initial value problem—I. *J. Atmos. Sci.*, 19 (1962), 329–341
- [23] F. Sorrentino and E. Ott, Using synchronization of chaos to identify the dynamics of unknown systems, *Chaos* 19 (2009), 033108
- [24] C. Sparrow, *The Lorenz Equations. Bifurcations, Chaos, and Strange Attractors*. Springer-Verlag New York Inc. 1982
- [25] C. Sparrow, An introduction to the Lorenz Equations, *IEEE Transactions on Circuits and Systems, CAS-30*, 8 (1983), 533–542
- [26] S. H. Strogatz, *Nonlinear dynamics and Chaos*, 2nd edition, Westview Press, 2015
- [27] M. Tao, *Hyperbolic periodic orbits in nongradient systems and small-noise-induced metastable transitions*, *Physica D: Nonlinear Phenomena*, 363 (2018) pp. 1-17
- [28] D. Viswanath, The fractal property of the Lorenz attractor, *Physica D* 190 (2004), 115–128
- [29] Structure of Lorenz attractors, *Publ. Math. I.H.E.S* 50 (1980) 59–72
- [30] J. A. Yorke and E. D. Yorke, *Metastable chaos: Transition to sustained chaotic behavior in the Lorenz model*, *J. Stat. Phys.*, 21 (1979), pp. 263–277
- [31] S. Yang, S. Potter, and M. Cameron, Computing the quasipotential for nongradient SDEs in 3D, *submitted* (2018), [arXiv: 1808.00562](https://arxiv.org/abs/1808.00562)